JOURNAL OF THERMOPHYSICS AND HEAT TRANSFER
Vol. 7, No. 3, July–Sept. 1993

Review of Chemical-Kinetic Problems of Future NASA Missions, I: Earth Entries

Chul Park
NASA Ames Research Center, Moffett Field, California 94035

Nomenclature

a = constant in Millikan-White correlation formula, Eq. (3)
b = constant in Millikan-White correlation formula, Eq. (3)
C = reaction rate constant, $cm^3 mole^{-1} s^{-1}$, Eq. (4)
C_d = parameter associated with turbulence decay rate
D = dissociation energy
D_a = characteristic Damköhler number, Eq. (10)
d = mixing length
f = normalized stream function
G = parameter associated with turbulence decay rate
h = normalized turbulence energy
k = Boltzmann constant
k_f = forward reaction rate coefficient, $cm^3 mole^{-1} s^{-1}$
M = unspecified third body
m = mass of a particle, g
N_e = electron density, cm^{-3}
n = pre-exponential temperature power, Eq. (4)
n_t = total number density, cm^{-3}
p = pressure, Pa or atm
Q = partition function
q_r = stagnation point radiative heat flux, W/cm^2
R = nose radius, m
r = radial distance, cm
s = exponent in average temperature, Eq. (1)
T = heavy particle translational-rotational temperature, K
T_a = geometric average temperature, K, Eq. (1)
T_d = activation temperature of reaction, K, Eq. (4)
T_e = electron temperature (set equal to T_v), K
T_v = vibrational (of neutral molecules)-electron-electronic temperature, K
T_v^* = vibrational temperature of N_2^+ (B) state defined by Eq. (8b), K
$T_v(B)$ = vibrational temperature of N_2^+ (B) state determined from $v = 0$ and $v = 1$ state populations, K
T_x = unspecified temperature (T, T_a, T_e, or T_v), K
u = velocity tangential to wall, cm/s
V = flight velocity, cm/s or km/s
v = velocity normal to wall, cm/s
ν = vibrational quantum number
W = species production rate, s^{-1}
α = species mass fraction
ε = turbulence energy
η = normalized distance normal to wall
θ = characteristic vibrational temperature, ω_e/k, K
μ = equivalent molecular weight, g/mole, or viscosity, poise
ξ = normalized distance along wall
ρ = density, g/cm^3
σ_v = collision-limiting cross section for vibrational relaxation, cm^2
τ_v = vibrational relaxation time, s
ω_e = vibrational constant, cm^{-1}

Subscripts

a = average value
e = edge of ablation product layer
f = forward reaction
r = reverse reaction
s = behind normal shock wave
t = turbulence
v = vibration
w = wall
∞ = freestream
1 = condition ahead of shock wave

Introduction

THE nonequilibrium thermochemical relaxation phenomena occurring behind a shock wave surrounding an object flying in the Earth's atmosphere have been studied intensely since the 1960s. Experimental observations of the phenomena have been made mainly using shock tubes. A great deal of data has been gathered for the vibrational relaxation rates at temperatures below about 5000 K over a wide range of pressures, and an excellent correlation formula based on the Landau-Teller theory has been found by Millikan and White[1] to represent them. The chemical reaction schemes and the as-

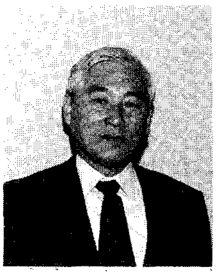

Chul Park is a Staff Scientist at the NASA Ames Research Center in the Aerothermodynamics Branch. He joined Ames Research Center in 1964. His pioneering works include conception and design of aeroassisted orbital transfer vehicles, for which he holds a patent, study of radiation and radiative transport in air not in thermodynamic equilibrium, environmental impact of Space Shuttle on ozone layer, and an impact of meteor penetration of Earth's atmosphere. He is the author of a book titled *Nonequilibrium Hypersonic Aerothermodynamics*, and authored or coauthored over 120 articles in scientific journals. The author received a B.S. (1957) and an M.S. (1960) in Aeronautical Engineering from Seoul University, Seoul, Korea, and a Ph.D. (1964) in Aeronautics (hypersonics) from Imperial College of Science and Technology, London, England. The author is an Associate Fellow of AIAA.

Presented as Paper 91-0464 at the AIAA 29th Aerospace Sciences Meeting, Reno, NV, Jan. 7–10, 1991; received April 3, 1992; revision received Sept. 11, 1992; accepted for publication Sept. 18, 1992.

sociated rate coefficients have been determined for postshock temperatures, before reaction, of up to about 15,000 K.

Experiments have also been conducted at AVCO Everett Research Laboratories, Everett, Massachusetts, and elsewhere during the 1960s to study the radiation phenomena for shock velocities of up to 12 km/s (e.g., Ref. 2). Postshock temperatures in these experiements were between 20,000–60,000 K. The most prominent feature observed in such studies at shock speeds below 10 km/s was that the radiation, which was found to emanate mostly from molecular species, is higher in the nonequilibrium region preceding the equilibrium region than in the equilibrium region downstream. That is, radiation overshoot occurs. The overshoot characteristics could not be explained by the reaction schemes and the rate coefficient sets derived from the experiments made at temperatures below 15,000 K.[3] According to the conventional (i.e., one-temperature) reaction scheme, the intensity of the molecular radiation should be the maximum immediately behind the shock wave where the temperature is the maximum. However, the experimental data showed that the radiation peak occurs a finite distance away from the shock wave. The attempt to attribute the slow occurrence of the peak to an incubation phenomenon of nonequilibrium vibrational excitation also failed, because the observed times to the peak radiation were much longer than the vibrational relaxation times calculated by the Millikan-White correlation formula.[3] Also, the times to reach equilibrium observed in the radiation experiments were much longer than the values calculated by the conventional theories. These anomalies were exacerbated by the lack of a rational means of calculating radiation under thermochemical nonequilibrium conditions.[3]

Recently, the slow relaxation and radiation overshoot have been explained using a theoretical multitemperature model in which the vibrational temperature T_v is recognized to be different from the translational and rotational temperatures. According to this model, at very high temperatures the vibrational relaxation phenomenon changes its character from the Landau-Teller type to a slower type that has been called a diffusion type.[3,4] In this model, the electron temperature and the electronic temperature are assumed, for the purpose of determining flow properties, to be equal to T_v, while the rotational temperature is equated to the translational temperature. The influence of the vibrational temperature on the rates of chemical reactions is accounted for by assuming that the rate coefficients for dissociation are functions of the geometrical mean temperature between T and T_v, i.e.

$$T_a = T^s T_v^{s-1} \tag{1}$$

where s is between 0.5–0.7. This model is named the two-temperature model.[3,4] A computer code that can determine the radiative properties of the gas under such a nonequilibrium condition has been developed and was named nonequilibrium air radiation (NEQAIR).[5]

Two computer codes have been written to calculate the one-dimensional flow in thermochemical nonequilibrium using the two-temperature model and to calculate radiation from it using NEQAIR: the code shock tube radiation program (STRAP) for the shock tube flow behind a normal shock wave and stagnation point radiation program (SPRAP) for the stagnation streamline in the shock layer over a spherical blunt body. The procedure for obtaining the flow properties along the stagnation streamline in the SPRAP code is described in Refs. 6 and 7. These two codes have been used to successfully reproduce most of the experimental radiation data taken in shock tubes, ballistic ranges, and flight experiments at shock velocities equal to or below about 10 km/s.[6,7] (An exception exists for the vibrational temperature, which will be discussed later). A set of dissociation rate coefficients compatible with this model has been derived from the existing experimental data in Ref. 8. The chemical reaction rate scheme used in these works will be referred to as the 1987 or the "old model," and their rate coefficients as the 1987 or the "old rates." More recently, the rate coefficient for electron-impact dissociation of N_2 was determined in Ref. 9. The STRAP and SPRAP were improved and combined into a single code named nonequilibrium (NONEQ).[10] The improvement consisted of 1) generalization of the chemical reaction schemes; 2) improvement of the accuracy of the partition functions and the radiation calculation routines; and 3) inclusion of the species C, CO, CN, and C_2 in the excitation calculation. Several two- or three-dimensional computer codes that incorporate the model have been developed over the years. Two of the most notable of these are given in Refs. 11 and 12. These codes have been tested for various conditions with generally satisfactory results, at least at flight velocities below 10 km/s.

At flight velocities above 10 km/s, all molecules quickly dissociate, and the radiation is emitted mostly by the atoms. Atomic radiation is a strong function of electron temperature and is proportional approximately to the square of electron density. The electron temperature and density are both affected by the nonequilibrium ionization processes. Thus, the problem of determining the radiation in this velocity range becomes one of correctly calculating the nonequilibrium ionization processes.

In air, electrons are produced first by the associative ionization process $N + O \rightarrow NO^+ + e^-$. The NO^+ ion so produced then transfers its charge to other neutral species through several charge-exchange reactions. When the resulting density of the electrons reaches a certain threshold value, the collisions of electrons with neutral N and O atoms begin to contribute significantly to the ion production. Since the number of electrons doubles in each such event, electron density increases exponentially when this happens, in the form of an avalanche. To describe these phenomena correctly, one must know the rate coefficients for the three types of ionic reactions: 1) associative ionization, 2) charge-exchange, and 3) the electron-impact ionization. At relatively low flight speeds (below about 6 km/s), only the first mechanism is present; at the intermediate flight speeds (between 6 and 10 km/s), the second mechanism is added to the first. At higher velocities, the third mechanism becomes important. The rate coefficients for the first and the third mechanisms are known to a limited extent, and the rate models in Refs. 6 and 7 represent the best available such data. The rates for the second mechanism, i.e., the charge-exchange reactions, have not been well-known until recently, and the rate coefficients for this mechanism used in Refs. 6 and 7 have been mostly the estimated values.

In the future, NASA may consider manned missions to the Moon and the planet Mars. In order to reduce the weight of vehicles for such missions, an aerobraking maneuver could be used for atmospheric entry. The lunar return produces an Earth entry velocity below 11 km/s, while the Mars-return entry will be at a super-escape velocity above 11.3 km/s, and possibly up to 14 km/s. In order to determine the radiative heat fluxes falling on the aerobrake under these conditions, one must first know the extent and possible impact of nonequilibrium ionization processes at these entry speeds.

Ionization phenomena have been studied experimentally since the 1950s at low and intermediate shock speeds. Wilson[13] observed, in a shock tube, the behavior of the electron density in the velocity range between 9–12 km/s. References 3–8 did not test Wilson's results because the rate coefficients for the ionic reactions were unreliable.

Very recently, the rate coefficients for the three ionic processes have been examined in Ref. 14. Therein, the rate coefficients for the associative ionization reactions and electron-impact ionization reactions have been determined from analysis of an up-to-date experimental data base. A set of charge-exchange rate coefficients have also been derived from the existing experimental data. Using these reaction rate coefficients, it is now possible to exercise the ionization model to see how well it reproduces the experimental data, and this is the first purpose of this article. Here, the rate coefficients affecting the ionic equilibration process are systematically varied to determine the values that reproduce Wilson's experimental data most closely. Using the rate coefficients so deduced, a radiation calculation is performed.

At the typical entry flight conditions for the Mars-return missions, the present work will show that the wall radiative heating rate is too high for a nonablating heat shield. When ablation occurs, one must examine the thermochemical and radiative phenomena occurring in the ablation-product, which is the second purpose of the present work. The study shows that the ablation-product gas is most likely in a chemical nonequilibrium state. The possibility of the presence of turbulence in the ablation-product layer is then discussed.

Vibrational Relaxation Parameters

In Ref. 1, it is shown that τ_v can be expressed in the form

$$p\tau_v = \exp[a(T^{-1/3} - b) - 18.42] \text{ atm} - \text{s} \tag{2}$$

Reference 1 also shows that the parameters a and b can be expressed for many gases by the simple expressions

$$\begin{aligned} a &= 0.00116\mu^{0.5}\theta^{1.333} \\ b &= 0.015\mu^{0.25} \end{aligned} \tag{3}$$

where μ is the equivalent molecular weight between the two colliding particles and θ is the characteristic vibrational temperature (the vibrational constant ω_e divided by the Boltzmann constant). References 15–17 show that the correlation formulas for a and b [Eq. (3)], do not reproduce the experimental data for the N_2-O, O_2-O, and NO-NO collisions. For these cases, a and b are obtained by fitting the experimental data to these collisions. The O_2-N collisions are assumed to produce the same a and b values as those for the N_2-O collisions; while the collisions of NO with N, O, N_2, and O_2 are assumed to produce the same a and b values as for the NO-NO collisions. The values of a and b so chosen, and their sources, are tabulated in Table 1.

References 3–12 and 14 show that the vibrational relaxation rates at high temperatures must be corrected to account for the limiting of the excitation rates due to the finiteness of the elastic collision cross sections. This is done by adding the time for the elastic collisions to the vibrational relaxation time in the form[3]

$$\tau(\text{total}) = \tau_v + [n_t\sqrt{(8kT/\pi m)}\sigma_v]^{-1}$$

where n_t and m are the total number of colliding particles and the average mass of the mixture, respectively. σ_v is represented by[6,7,14]

$$\sigma_v = \sigma_v'(50{,}000/T)^2 \text{ cm}^2$$

The σ_v' values for N_2, O_2, and NO are all chosen to be 3×10^{-17} cm^2.

Table 1 Vibrational constants a and b for N_2, O_2, and NO

		a	b	Source
N_2				
	M^a = N	180	0.0262	Eq. (3)
	O	72.4	0.0150	Ref. 15
	N_2	221	0.0290	Eq. (3)
	O_2	229	0.0295	Eq. (3)
	NO	225	0.0293	Eq. (3)
O_2				
	M^a = N	72.4	0.015	Assumed to be same as for N_2-O
	O	47.7	0.059	Ref. 16
	N_2	134	0.0295	Eq. (3)
	O_2	138	0.0300	Eq. (3)
	NO	136	0.0298	Eq. (3)
NO				
	M^a = N	49.5	0.042	Assumed to be same as for NO-NO
	O	49.5	0.042	Assumed to be same as for NO-NO
	N_2	49.5	0.042	Assumed to be same as for NO-NO
	O_2	49.5	0.042	Assumed to be same as for NO-NO
	NO	49.5	0.042	Ref. 17

[a] M designates colliding species.

Reaction Rate Coefficients

As stated in the Introduction, experimental data in the super-escape velocity range have been obtained by Wilson.[13] In Fig. 1, the oscilloscope traces of the radiation observed at two wavelengths by Wilson are reproduced.[13] In each of the three traces, the upper trace shows the intensity of radiation observed at around 5000 Å, while the lower trace is that at around 6.1 μ. As was stated in Ref. 13, the intensity of radiation at 6.1 μ is approximately proportional to the square of electron density. The 5000-Å radiation was observed by Wilson in order to detect the location of the shock wave. Since the absolute density of the gas flow behind the shock wave was low in Wilson's experiment, it was not possible to determine the location of the shock wave through an independent measurement. Wilson deduced the location of the shock wave from the peak point in the radiation at 5000 Å. In measurements that preceded Wilson's, the radiation overshoot phenomena had been studied extensively at shock speeds below 10 km/s, and thus, the distance between the radiation peak point and the shock wave was well-characterized for this velocity range.[2] Wilson extrapolated this radiation peak point relationship to shock velocities above 10 km/s. Both the 5000-Å and the 6.1-μ radiations exhibit a plateau for a sufficiently long period of time, followed by a sudden increase in intensity. The plateau is believed to represent the equilibrium region, while the rise is due to the onset of the contact surface.

In order to numerically reproduce Wilson's results, calculations have been performed in the present work using the computer code NONEQ mentioned earlier. As described in Ref. 4, the code accounts for all aspects of ionization process in detail, and therefore is valid over a wide range of ionization fraction considered in the present work. The only significant assumption in the code concerns radiative cooling phenomenon, which will be discussed later. The exponent s in Eq. (1) was chosen to be 0.5, because this was the value used in

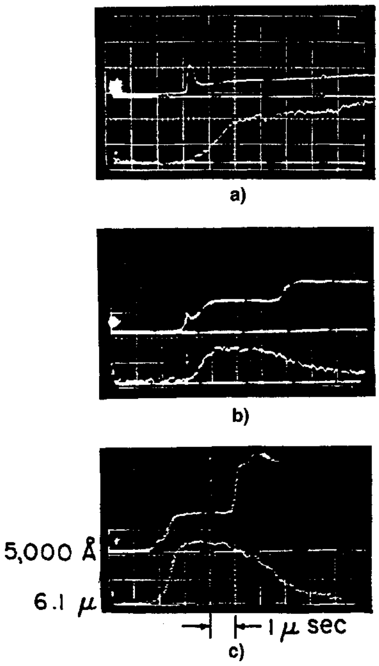

Fig. 1 Oscilloscope records of radiation intensities at 5000 and 61,000 Å obtained in a shock tube[13]: a) p_1 = 26.7 Pa (0.2 Torr), V = 9.5 km/s; b) p_1 = 13.3 Pa (0.1 Torr), V = 10.9 km/s; and c) p_1 = 13.3 Pa (0.1 Torr), V = 11.25 km/s.

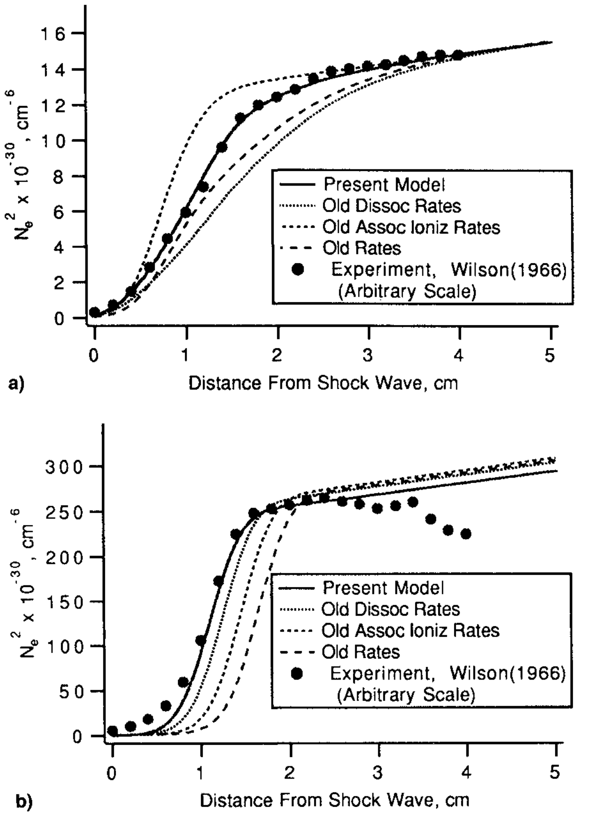

Fig. 2 Comparison between the experimental data[13] and the present calculation on 61,000-Å radiation showing the impact of various rate coefficients: a) p_1 = 26.7 Pa (0.2 Torr), V = 9.5 km/s; b) p_1 = 13.3 Pa (0.1 Torr), V = 11.25 km/s.

Ref. 7, and because the present work uses basically the same rate parameters except for those described below. The calculations were made first using the rate coefficients given in Ref. 14. The results are shown in Figs. 2a and 2b marked as the old rates, and compared with the experimental data. As seen in these figures, there is a discrepancy between the theory and experiment. To reduce the discrepancy, a systematic variation of the rate coefficients was made. First, radiative recombination processes are added to the old reaction scheme. The recombination rate coefficients are calculated using the NEQAIR code.[5] (The NEQAIR code has a provision which enables calculation of electron-impact ionization and radiative recombination rates of neutral atoms.) It was first found that varying the charge-exchange rate coefficients had little impact on the calculated results, and so the rate coefficients in Ref. 14 are retained for the charge-exchange reactions. However, the reaction $N^+ + N_2 \rightarrow N + N_2^+$ was added to the scheme because this is missing in the reaction scheme given in Ref. 14. It is conventional to express a reaction rate coefficient in the form

reaction rate coefficient

$$k_f = CT_x^n \exp(-T_d/T_x) \tag{4}$$

where T_x is a yet unspecified controlling temperature, which may be T, T_a, T_e, or T_v. In this convention, the rate coefficient for the nitrogen charge exchange process was estimated in this work to be

$N^+ + N_2 \rightarrow N + N_2^+$:

$$k_f = 10^{12} T^{0.5} \exp(-12200/T) \text{ cm}^3\text{mole}^{-1}\text{s}^{-1}$$

The n value of 0.5 is from the assumption of a fixed reaction cross section, and the preexponential power factor C chosen is a median value for such reactions.

Equilibration rate calculations revealed that the electron-impact ionization rates have little impact on the rate of ionization equilibration because of the loss of electron thermal energy during the electron-impact ionization process. (Electron-impact ionization results in the ionization of an atom at the expense of the electrons' thermal energy; see Chap. 4 of Ref. 14.) The larger its rate coefficient, the more the electron thermal energy is suppressed during ionization, and the ionization reaction is slowed down. Therefore, the rates used in Refs. 6 and 7 and adopted in Ref. 14 are also used in the present work. (There is a typographical error in Ref. 14 for the nitrogen ionization rates: the C value for nitrogen ionization used in Refs. 6 and 7 should be 2.5×10^{34}, not 2.5×10^{33}, as given in Ref. 14.)

The rate coefficients for the nitric oxide exchange reactions given in Ref. 14 are well-established, and therefore are unchanged in this study. Systematic study revealed that the ionization profiles are affected mostly by the associative ionization rates. In Sec. 8.2 of Ref. 14, it is shown that the existing experimental data for the three associative ionization processes (for NO^+, O_2^+, and N_2^+) would lead to the expressions

$N + O \rightarrow NO^+ + e^-$:

$$k_f = 5.28 \times 10^{12}(T/6000)\exp(-31{,}900/T) \tag{5}$$

$N + N \rightarrow N_2^+ + e^-$:

$$k_f = 2.04 \times 10^{13}(T/6000)^{1.5} \exp(-67{,}500/T) \tag{6}$$

$O + O \rightarrow O_2^+ + e^-$:

$$k_f = 1.12 \times 10^{13}(T/6000)^{2.7} \exp(-80{,}600/T) \tag{7}$$

The n value in these expressions are all equal to, or greater than, +1. In Ref. 14, it was argued that values for n equal to or greater than +1 are unlikely, and therefore, they should be set to zero. Furthermore, the controlling temperature was changed from T to T_a, with the speculation that the reactions are affected by the vibrational temperature to the same extent as are the dissociation reactions. In the present work, both sets of these rate coefficients are tested. It was found that the uncorrected expressions [Eqs. (5–7)] yield better agreement with Wilson's data than do the modified values given in Ref. 14. Hence, these rate coefficients are selected for the present model, and are listed in Table 2. The rate coefficients selected in the present work [Eqs. (5–7)] are compared with those in Ref. 14 in Fig. 3. As the figure shows, the two sets are approximately equal in the low temperature range, but differ considerably at high temperatures. The reason why Eqs. (5–7) yield better agreement with experiment is yet unknown, and should be investigated in the future.

In Figs. 2a and 2b, the comparison is made between the experimental data and the present calculations. In the figure, the curves labeled "old dissoc rates" refer to the calculations in which the new rates are used, except for the dissociation rates of O_2 and NO. There are minor, but discernible differences. Likewise, the "old ionization rates" refers to the calculations in which the new rates are used, except for the associative ionization rates for which the old rates values are used. As seen in the figures, for both the 9.5 and the 11.25 km/s cases, the new rates yield better agreement with the experiment.

In Figs. 4a and 4b, the results of calculations are shown in which the rate coefficients for the associative ionization are increased and decreased by a factor of 10. As seen here, factor of 10 changes in either direction cause discernible changes in the calculated N_e^2 profiles.

In Figs. 5a and 5b, a comparison is made between the measured and the calculated intensities of the 5000-Å radiation. As seen in the figures, the calculated and the measured values agree in the region immediately behind the shock wave,

Table 2 Reaction rate coefficients for air (present model)

Reaction	M	T_x[a]	C	N	T_d	Source
Dissociation reactions						
$N_2 + M \rightarrow N + N + M$	N	T_a	3.0^{22}	−1.60	113,200	Ref. 14
	O		3.0^{22}			
	N_2		7.0^{21}			
	O_2		7.0^{21}			
	NO		7.0^{21}			
	N^+		3.0^{22}			
	O^+		3.0^{22}			
	N_2^+		7.0^{21}			
	O_2^+		7.0^{21}			
	NO^+		7.0^{21}			
	e^-		1.2^{25}			Ref. 9
$O_2 + M \rightarrow O + O + M$	N	T_a	1.0^{22}	−1.50	59,500	Ref. 14
	O		1.0^{22}			
	N_2		2.0^{21}			
	O_2		2.0^{21}			
	NO		2.0^{21}			
	N^+		1.0^{22}			
	O^+		1.0^{22}			
	N_2^+		2.0^{21}			
	O_2^+		2.0^{21}			
	NO^+		2.0^{21}			
$NO + M \rightarrow O + O + M$	N	T_a	1.1^{17}	0.00	75,500	Ref. 14
	O		1.1^{17}			
	N_2		5.0^{15}			
	O_2		5.0^{15}			
	NO		1.1^{17}			
	N^+		1.1^{17}			
	O^+		1.1^{17}			
	N_2^+		5.0^{15}			
	O_2^+		5.0^{15}			
	NO^+		5.0^{15}			
NO Exchange reactions						
$NO + O \rightarrow N + O_2$		T	8.4^{12}	0.00	19,450	Ref. 14
$N_2 + O \rightarrow NO + N$		T	6.4^{17}	−1.00	38,400	Ref. 14
Associative ionization reactions						
$N + O \rightarrow NO^+ + e^-$		T	8.8^{8}	1.00	31,900	This work
$O + O \rightarrow O_2^+ + e^-$		T	7.1^{2}	2.70	80,600	This work
$N + N \rightarrow N_2^+ + e^-$		T	4.4^{7}	1.50	67,500	This work
Charge exchange reactions						
$NO^+ + O \rightarrow N^+ + O_2$		T	1.0^{12}	0.50	77,200	Ref. 14
$N^+ + N_2 \rightarrow N_2^+ + N$		T	1.0^{12}	0.50	12,200	Ref. 14
$O_2^+ + N \rightarrow N^+ + O_2$		T	8.7^{13}	0.14	28,600	Ref. 14
$O^+ + NO \rightarrow N^+ + O_2$		T	1.4^{5}	1.90	26,600	Ref. 14
$O_2^+ + N_2 \rightarrow N_2^+ + O_2$		T	9.9^{12}	0.00	40,700	Ref. 14
$O_2^+ + O \rightarrow O^+ + O_2$		T	4.0^{12}	−0.09	18,000	Ref. 14
$NO^+ + N \rightarrow O^+ + N_2$		T	3.4^{13}	−1.08	12,800	Ref. 14
$NO^+ + O_2 \rightarrow O_2^+ + NO$		T	2.4^{13}	0.41	32,600	Ref. 14
$NO^+ + O \rightarrow O_2^+ + N$		T	7.2^{12}	0.29	48,600	Ref. 14
$O^+ + N_2 \rightarrow N_2^+ + O$		T	9.1^{11}	0.36	22,800	Ref. 14
$NO^+ + N \rightarrow N_2^+ + O$		T	7.2^{13}	0.00	35,500	Ref. 14
Electron-impact ionization reactions						
$O + e^- \rightarrow O^+ + e^- + e^-$		T_e	3.9^{33}	−3.78	158,500	Ref. 14
$N + e^- \rightarrow N^+ + e^- + e^-$		T_e	2.5^{34}	−3.82	168,600	Ref. 14
Radiative recombination reactions						
$O^+ + e^- \rightarrow O + h\nu$		T_e	1.07^{11}	−0.52		This work
$N^- + e^- \rightarrow N + h\nu$		T_e	1.52^{11}	−0.48		This work

[a] T_x is the controlling temperature, C is in cm^3 $mole^{-1}$ s^{-1}.

but disagree considerably at large distances from the shock wave. The calculated intensity profile for the 9.5 km/s case show a gradual decrease toward a plateau past the peak point, in agreement with the observation by Allen.[2] Wilson's experimental data differ from the present calculation, and therefore, by implication, from the experimental data of Allen. This difference is believed to be due to the impurities present in Wilson's experimental environment. Impurities may have existed equally in Allen's experiment. However, Allen's radiation measurement was made at a wavelength of 5500 Å, and longer where N_2 tends to radiate strongly (by the N_2 first positive system). At the 5000-Å wavelength where Wilson made his measurement, the N_2 radiation is very weak, and hence, the contribution from impurities could have been significant. It is well-known that a shock tube made of stainless-steel produces a considerable amount of impurity in the test

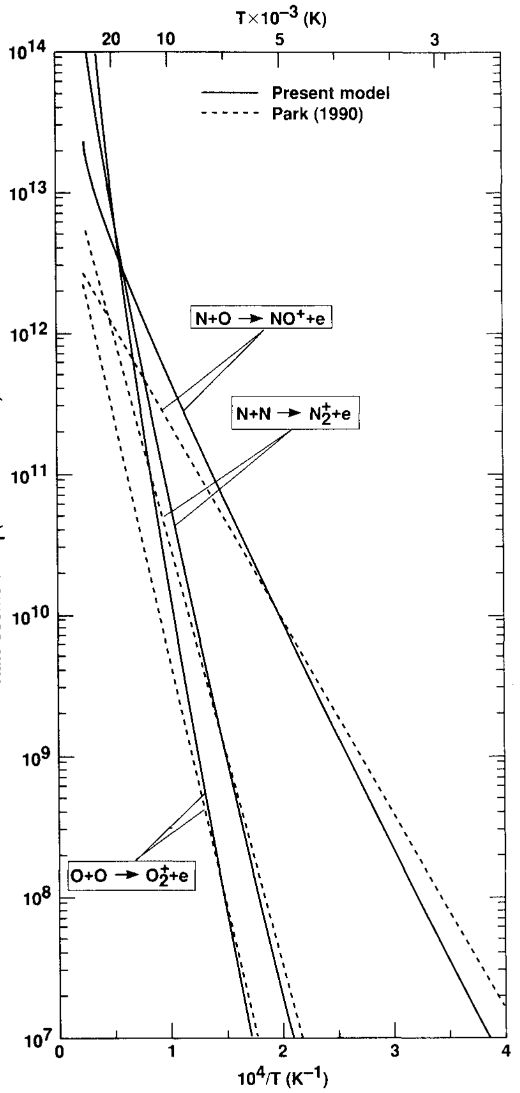

Fig. 3 Comparison between the associative ionization rate coefficients selected in the present work for air and those given by Park.[14]

gas, consisting mostly of iron, and that it emits strong radiation (e.g., Ref. 18). Presumably, iron is contained in various forms of compounds. It requires a finite time for the compounds to decompose and become electronically excited.

In Fig. 6, the electron mole fraction variation is calculated using the "present model" at 8 and 12 km/s for the freestream pressure p_1 of 0.5 and 0.1 Torr, respectively. This figure shows a distinct difference in the behavior of electron mole fraction. For the 8 km/s case, the electron density reaches a peak early, and decays to a plateau. The peak is caused by the overshoot of the associative ionization processes due to the high temperature in the early period. For the 12 km/s case, there is a peak in the early region also, but electron density climbs further to reach a second peak and a plateau. The first peak is due to the associative ionization processes, and the second peak is attributed to the electron-impact ionization processes.

Using the present model, the characteristic distance for ionization is calculated. The ionization distance is defined in the same manner as in the work of Wilson, i.e., by fitting a straight line to the rising portion of the N_e^2 variation, and extrapolating until it intersects with the peak value as shown in the inset in Fig. 7. The ionization distances are then divided by the mean free path ahead of the shock wave, as determined using a hard-sphere model, which, for the case of air, becomes

$$\text{mean free path} = \frac{1.62 \times 10^{14}}{\text{total number density in cm}^{-3}}$$

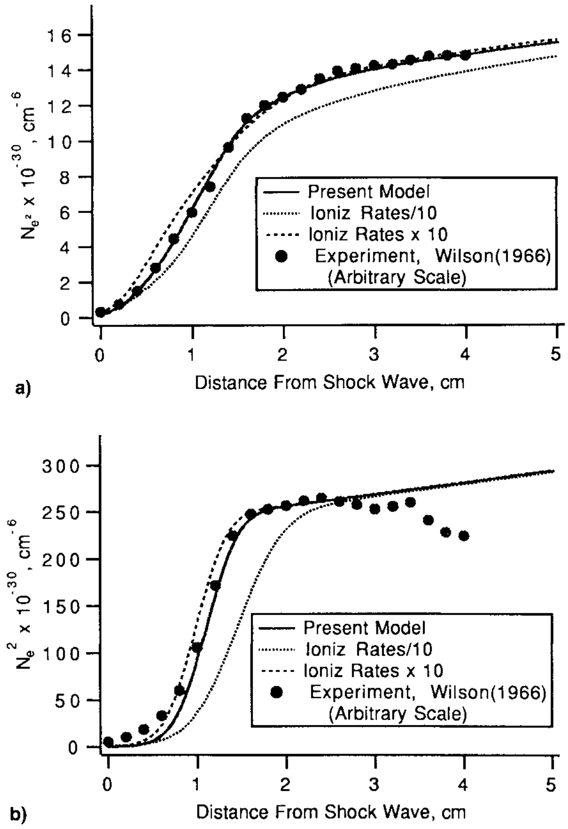

Fig. 4 Comparison between the experimental data[13] and the present calculation on 61,000-Å radiation showing the impact of associative ionization rate coefficients: a) p_1 = 26.7 Pa (0.2 Torr), V = 9.5 km/s; b) p_1 = 13.3 Pa (0.1 Torr), V = 11.25 km/s.

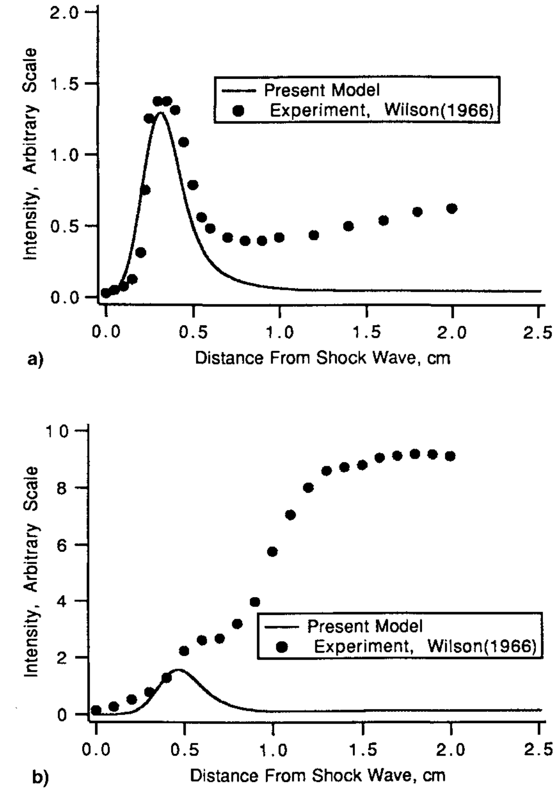

Fig. 5 Comparison between the experimental data[13] and the present calculation on 5000-Å radiation showing the impact of iron impurities: a) p_1 = 26.7 Pa (0.2 Torr), V = 9.5 km/s; b) p_1 = 13.3 Pa (0.1 Torr), V = 11.25 km/s.

In Fig. 7, the ratios of the ionization distance to the mean free path are compared between the existing experimental data and the present calculation. The experimental data are from Refs. 13 and 19–22. As seen in the figure, the calculation approximately reproduces the trend observed experimentally. The ionization distance is the shortest at 7 km/s, and exhibits a peak at 10 km/s. The experimental values are larger than the calculated values in the velocity range from 4 and 7 km/s. This may be attributed at least partly to the lack of spatial resolution and impurities in the experiment. At the speeds higher than 10 km/s, the experimental data are slightly smaller than the calculated values. This is most likely due to uncertainty in the location of the shock wave in the experiment: as indicated in the inset in Fig. 7, the experimental ionization distances exclude the ionization induction region, i.e., the region of relatively slow rise in electron density, and therefore is bound to be smaller than the true distance.

In Fig. 8, the calculated ionization equilibration times, defined as in Fig. 7, are compared with the two well-known characteristic relaxation times for radiation[6,7,14]: the time to the peak and the time for the equilibration of radiation observed at a wavelength of 5500 Å. As in the earlier reports, these times are given in the shock-tube coordinates, that is, they are the times measured by a stationary detector observing a passing flow. In order to determine the true time, one must multiply it by the density ratio ρ_s/ρ_1. The relaxation distances are found by multiplying the relaxation times by the shock speed. As seen in the figure, the ionization times are longer than the equilibration times for the 5500-Å radiation for velocities above 10 km/s. This is because ionization equilibration occurs after the radiation peak, as seen in Figs. 5a and 5b and 6. Figure 8 also shows the peak and the equilibration times below 10 km/s calculated using the present model. As seen here, there is an insignificant difference between the values calculated by the present model and those obtained by the old (1987) model.

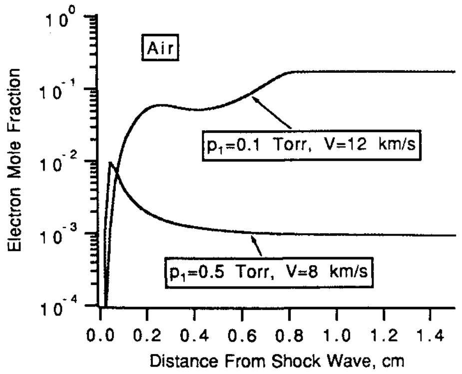

Fig. 6 Calculated electron mole fractions behind a shock wave at 8 and 12 km/s.

Figures 7 and 8 validate the thermochemical parameters chosen in the present work. However, one notes here that these parameters cannot be considered necessarily accurate or unique, because arbitrary choice had been made on several such parameters, purely empirically without rational reasoning. There could be one or more sets of thermochemical parameters different from the present values that would lead to an equally good agreement with the experimental data.

The properties behind a normal shock are calculated with the code NONEQ for the freestream density of 10^{-4} kg/m^3 and the velocity of 12 km/s. The selected combination of density and velocity results in a postshock pressure of about 0.15 atm. This pressure is selected because radiative heating of the Mars-return vehicle at the stagnation point is approximately at its maximum (e.g., Ref. 23) at this pressure. The results are shown in Figs. 9a and 9b. Unlike those given in Refs. 6 or 7, the present result shows a slight inflection in the decay of T at the distance of around 0.8 cm (see Fig. 9a). The process of ionization equilibration, seen in Fig. 9a, is slower than can be extrapolated from the equilibration time for the 5500-Å radiation. Ionization equilibration is reached at a distance of about 1.5 cm for this case.

In Figs. 10a and 10b, the results of a similar calculation made using the conventional one-temperature model are shown. The calculation is made using the same set of reactions and rate coefficients as for the two-temperature calculations described above, assuming that the vibrational-electronic temperature is the same as the translational-rotational temperature. The figures show that the equilibrium temperature is reached within about 0.05 cm, while the equilibrium compositions are reached within about 0.15 cm (except for N_2 which reaches equilibrium at about 0.25 cm). These equilibration distances are an order of magnitude shorter than those for the two-temperature model, and are believed to be erroneous.

In Fig. 11, the ionization equilibration distances, defined as in Fig. 7, are shown for the velocity range of 10–14 km/s with the postshock pressure p_s of 0.15 atm. The calculated

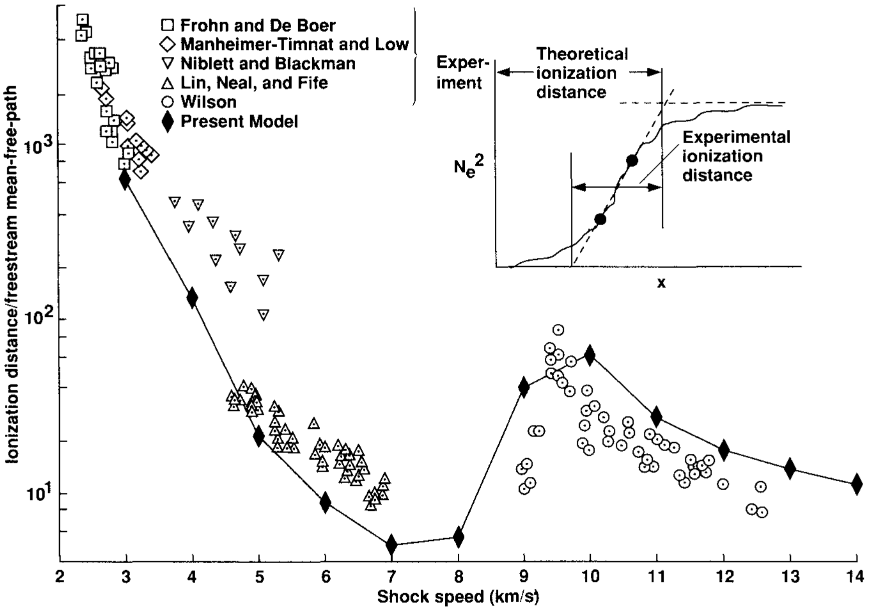

Fig. 7 Comparison between the ionization distances predicted by the present model and the experimental data.[13,19–22]

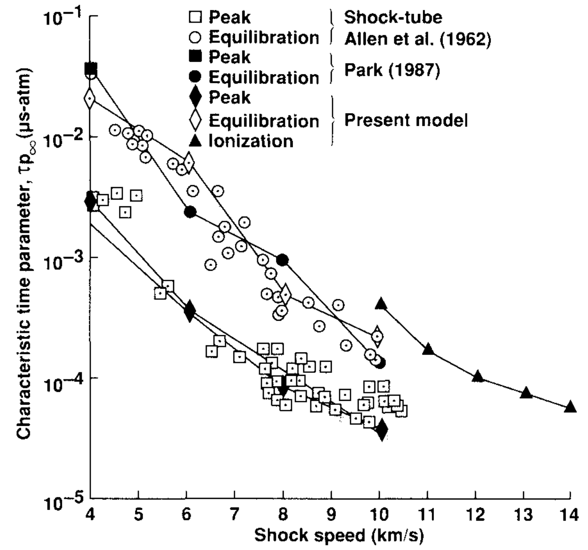

Fig. 8 Comparison between the ionization time and other characteristic relaxation times.

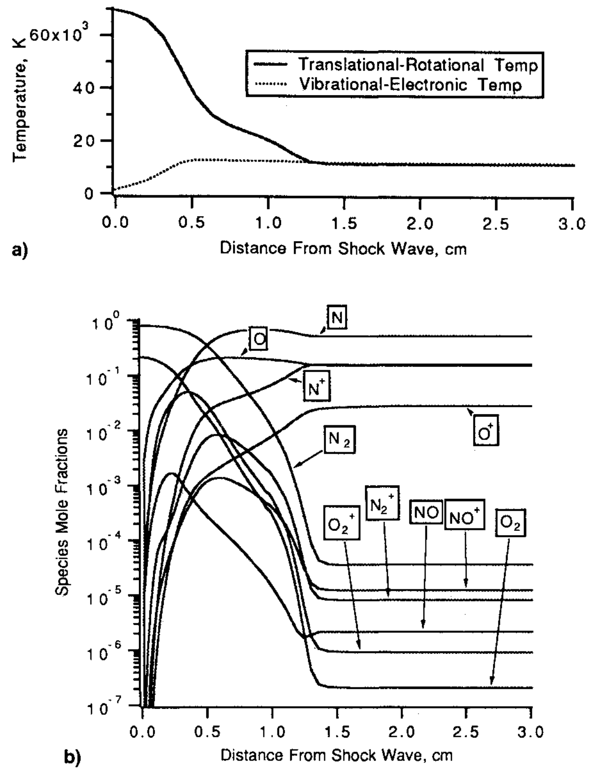

Fig. 9 Variation in thermodynamic properties behind a shock wave calculated by the two-temperature model, for $\rho_\infty = 10^{-4}$ kg/m^3 and $V = 12$ km/s: a) temperatures and b) species mole fractions.

ionization distances are between 1–2 cm. The data can be extrapolated to other density regimes using the binary scaling law, i.e., the equilibration distance is inversely proportional to flow density. In this case, the relaxation distance for ionization equilibration also means the relaxation distance for radiation equilibration, because in this flow regime, radiation intensity is proportional approximately to a square of electron density.

The two-temperature model developed in Refs. 4–8 failed to explain the experimental data by Allen[24] concerning vibrational temperature. The T_v calculated in STRAP, SPRAP, and NONEQ is that of the ground electronic states, X states, of the neutral molecules such as N_2, O_2, or NO. In the work of Allen, vibrational temperature in nitrogen was determined experimentally from the ratio of the intensities of radiation emanating from the $v = 1$ and the $v = 0$ states of the upper electronic state ($B^2\Sigma_u^+$) of the N_2^+ "first negative" system. The experimental values of the vibrational temperature so determined rose much more slowly than the calculated T_v.[6] This discrepancy is shown in Fig. 12. More recently, Sharma and Gillespie[25] measured the vibrational temperature of the N_2 "second positive" system which emanates from the $B^3\Pi$ state of N_2. Their measured value was closer to the calculated T_v. However, it was not understood why the N_2^+ vibrational temperature rises so slowly.

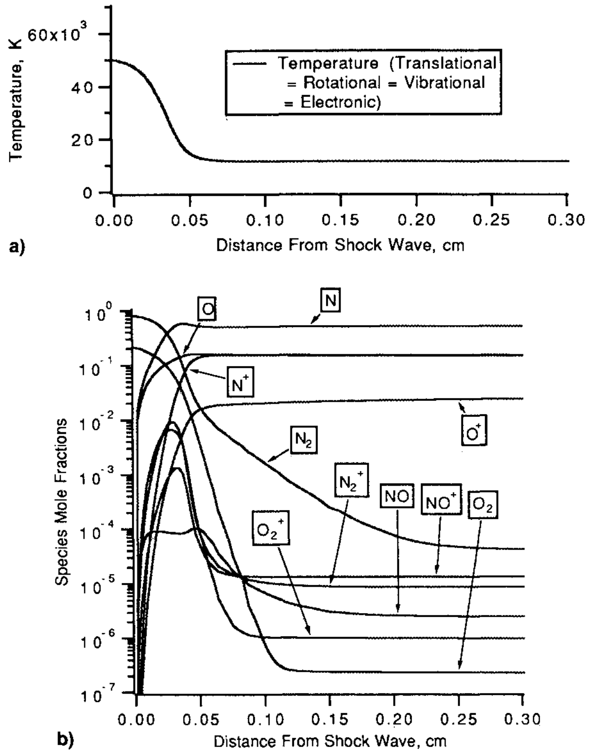

Fig. 10 Variation in thermodynamic properties behind a shock wave calculated by the one-temperature model, for $\rho_\infty = 10^{-4}$ kg/m^3 and $V = 12$ km/s: a) temperatures and b) species mole fractions.

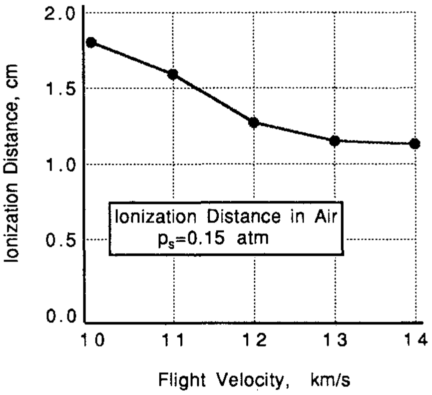

Fig. 11 Calculated ionization distances for air at $p_s = 1.52 \times 10^4$ Pa (0.15 atm).

To understand the cause of this discrepancy, one first constructs a population distribution diagram in a semilog plot as shown schematically in Fig. 13. If a Boltzmann distribution exists among the vibrational states, the number densities will form a straight line here. In a nonequilibrium environment, the distribution is curved in general as shown. The shaded area above the dissociation limit indicates the continuum nature of the free state $N + N^+$. The high vibrational states are

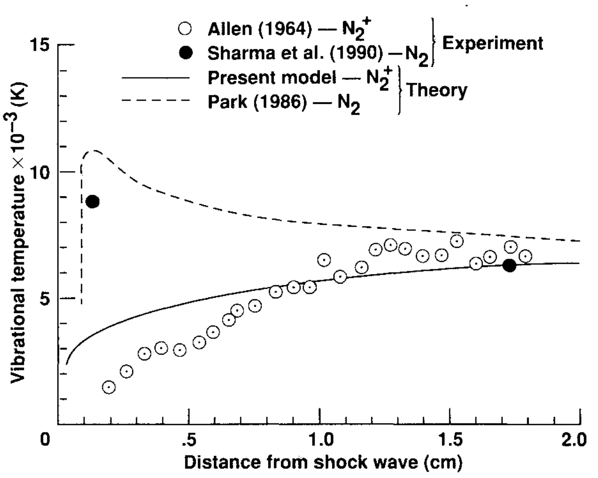

Fig. 12 Comparison between the vibrational temperature of N_2^+ predicted by the present model and those obtained by experiments.[24,25]

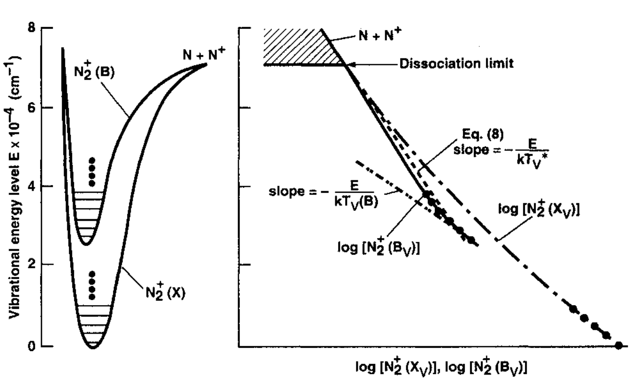

Fig. 13 Schematic of the plot of vibrational population distribution for N_2^+ $B^2\Sigma_u^+$ and $X^2\Sigma_g^+$ states in nonequilibrium environment.

in equilibrium with the free state due to the fact that the energy gap between the vibrational states and the free state is small. The vibrational temperature determined by Allen,[24] designated in the figure as $T_v(B)$, corresponds to the slope of the line connecting the ground and the first excited vibrational states of the $N_2^+(B)$ state. In a nonequilibrium environment, the vibrational temperature for N_2^+ is not expected to necessarily agree with that of N_2 measured by Sharma and Gillespie.[25]

If one represents the curved vibrational distribution of $N_2^+(B)$ approximately by a straight line, shown as a dashed line in the figure, then one gains an insight into the time scale of change of the observed $T_v(B)$. Such a straight-line distribution can occur even under a nonequilibrium environment if the cross sections for the collisional transitions between the neighboring vibrational states are very large. Because the high states are in equilibrium with the free state $N + N^+$, the condition that the distribution be a straight line demands that all states be in equilibrium with the free state. Let us assign a temperature T_v^* to characterize this quasi-Boltzmann distribution. Then the straight-line distribution can be represented by the condition of equilibrium between an arbitrary state v and the free state in the form

$$\frac{(N)(N^+)}{[N_2^+(B_v)]} = \frac{Q(N)Q(N^+)}{Q[N_2^+(B_v)]} \exp[-D(B_v)/T_v^*] \qquad (8a)$$

Here, (N), (N^+), and $[N_2^+(B_v)]$ are the number densities of the respective species, $Q(N)$, $Q(N^+)$, and $Q[N_2^+(B_v)]$ are the partition functions of the species in reference to their respective ground states, and $D(B_v)$ is the dissociation energy of the $N_2^+(B)$ molecule in its vth vibrational state. For the evaluation of $Q(N)$, $Q(N^+)$, and $Q[N_2^+(B_v)]$, the translational temperature T is used for the evaluation of the translational and rotational components, and T_v^* is used for the vibrational component. By taking the reciprocals of the two sides in Eq. (8a), and by summing them over v and by taking the reciprocals of the resulting sums, one obtains

$$\frac{(N)(N^+)}{[N_2^+(B)]} = \frac{Q(N)Q(N^+)}{Q[N_2^+(B)]} \exp[-D(B_0)/T_v^*] \qquad (8b)$$

where $N_2^+(B)$ and $Q[N_2^+(B)]$ are the number density of the N_2^+ molecule in the B state and its partition function measured from the ground vibrational state of the B state, respectively, and $D(B_0)$ is the dissociation energy measured from the ground vibrational state of the B state. One can solve Eq. (8b) for T_v^* from the given (N), (N^+), and $[N_2^+(B)]$. T_v^* is then a function of the number density of the ion, N^+, and is in general different from $T_v(B)$.

In Fig. 12, T_v^* deduced from Eq. (8b), is presented as the present model and is compared with the measurement by Allen $[T_v(B)]$. As seen here, the present model leads to a time-scale of change that agrees with that of the measurement, though, as expected, the two temperatures are different. The time-scale of change of both these vibrational temperatures is dictated by that of N^+ concentration. This implies that the vibrational temperatures deduced from the N_2^+ "first negative" emissions are unrelated to the vibrational temperature of the neutral species N_2. If the v-v transfer (energy transfer between the vibrational mode of one molecule to that of another) between N_2^+ and N_2 were sufficiently strong to prevent establishment of Eq. (8a) and to bring the $N_2^+(B)$ distribution to align with the N_2 distribution, then the two temperatures [T_v^* and $T_v(B)$] could both conceivably approach the vibrational temperature of N_2. However, apparently that is not the case.

Radiation

In Ref. 7, the radiative heat fluxes incident on the wall at the stagnation point in the wavelength range above about 2000 Å have been calculated using the old (1987) model using the SPRAP code. The calculation procedure for the stagnation point is described in Refs. 6 and 7. In order to test the impact of the changes made in the vibrational and reaction rate parameters in the present work, a similar calculation has been made in the present work using the NONEQ code.[10] The calculation was made for a body of 1-m radius, over the velocity range from 10 to 14 km/s. The freestream density was fixed at 10^{-4} kg/m^3. The postshock pressures corresponding to 10 and 14 km/s are 0.1 and 0.2 atms, respectively. These pressures are nearly the same as those in the shock tube experiment of Wilson.[13] Radiative cooling of the flow is partially accounted for by assuming that the photons emitted by the bound-free radiative recombination processes escape from the system. This assumption is believed to account for at least $\frac{2}{3}$ of the radiative cooling in the highly ionized regime. The wall is assumed to be nonablating and nonreflecting, and is at 1800 K, which is a typical temperature of heated nonablating heat shield in flight. The results are compared in Fig. 14 with those given in Ref. 7. As seen in this figure, there is only a small difference (typically about 20%) between the two sets of calculations for the chosen value of $\rho_\infty R$.

For the same shock layer flowfield, radiative transfer calculations were carried out through a line-by-line technique, fully accounting for all absorption phenomena. The resulting spectra are compared for the 10 and the 12 km/s cases in Fig. 15. As seen here, the two cases show approximately the same magnitudes of the N_2^+ radiation between the wavelengths of 3000–4500 Å. Elsewhere, there is a marked difference, especially in the vacuum-ultraviolet wavelength range below 2000 Å. For the 10 km/s case, even the strongest radiation in this wavelength range, which is at 1745 Å, is below the minimum scale. For the 12 km/s case, there are many other atomic lines from N and O and their bound-free continua in the

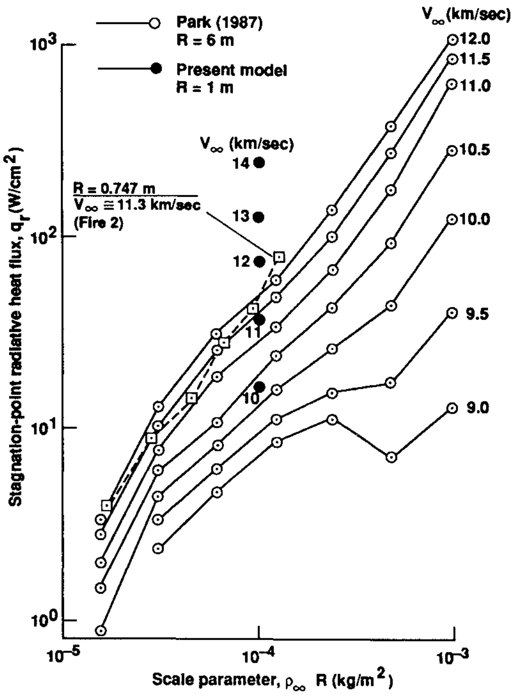

Fig. 14 Calculated optically-thin radiative heat flux at wavelengths greater than 2000 Å at the stagnation point of a spherical body.

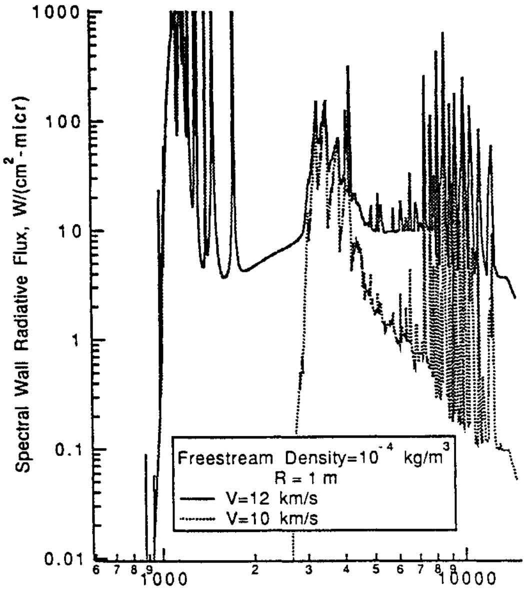

Fig. 15 Calculated spectral radiative flux incident on the stagnation point wall for a body of $R = 1$ m at $\rho_\infty = 10^{-4}$ kg/m^3 and $V = 10$ and 12 km/s.

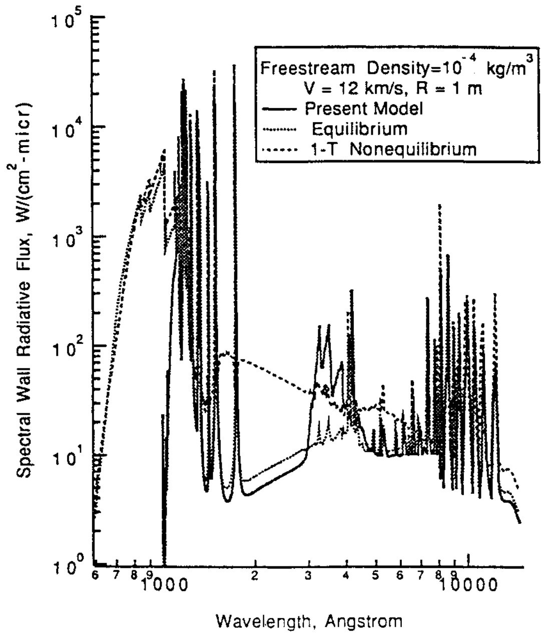

Fig. 16 Calculated spectral radiative flux incident on the stagnation point wall for a body of $R = 1$ m at $\rho_\infty = 10^{-4}$ kg/m^3 and $V = 12$ km/s, obtained with both two-temperature nonequilibrium model and equilibrium model.

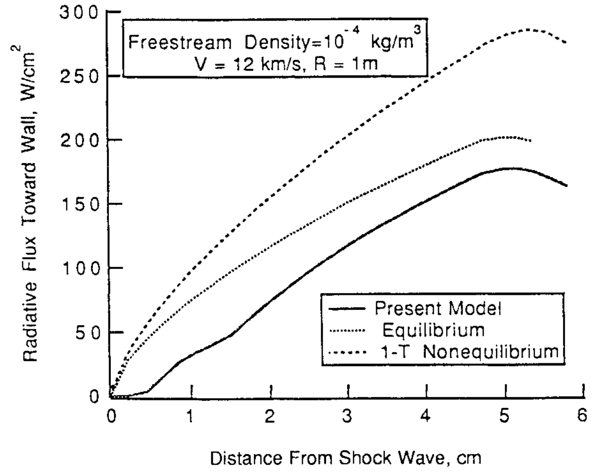

Fig. 17 Calculated variation of radiative heat flux along the stagnation streamline for a body of $R = 1$ m at $\rho_\infty = 10^{-4}$ kg/m^3 and $V = 12$ km/s, obtained with both two-temperature nonequilibrium model and equilibrium model.

vacuum-ultraviolet wavelength region (the free-free continuum is negligible at these wavelengths).

The 12 km/s case was calculated also assuming the shock layer to be in equilibrium, and using the one-temperature model, for the nose radius of $R = 1$ m. The resulting spectra are compared with the nonequilibrium case in Fig. 16. As seen in the figure, the equilibrium and the one-temperature cases produce discernibly greater radiation than the nonequilibrium case at wavelengths below about 1200 Å, for the nose radius of 1 m. The radiation in this short wavelength range originates mostly in the bound-free continuum, and its emission power is proportional approximately to the square of electron density and the thickness of the emitting region. The equilibrium solution yields a thicker region of high-electron density than the nonequilibrium solution, and this causes the increase in the wall radiative heat flux. Another interesting point is that the one-temperature nonequilibrium model predicts the continuum radiation above about 1500 Å to be significantly larger than that from the two-temperature or the equilibrium case. This is because the electron temperature predicted in the one-temperature model is higher than in the other models.

In Fig. 17, the radiative heat flux in the direction toward wall, q_r, is compared between the present two-temperature, equilibrium, and one-temperature nonequilibrium cases along the stagnation streamline. For the present two-temperature nonequilibrium case, radiative flux starts at a distance of about 0.5 cm. This is because of the low degree of ionization in the region immediately behind the shock wave. In the other two cases, radiative flux starts to rise immediately from $x = 0$. At the wall, which is at approximately 6 cm for the nonequilibrium and 5.4 cm for the equilibrium flow according to this model, the radiative flux for the equilibrium flow is slightly higher than the present model, but the one-temperature nonequilibrium case leads to a substantially higher flux value.

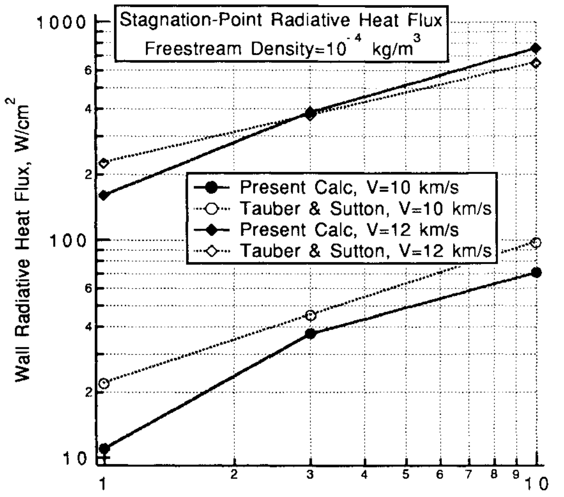

Fig. 18 Comparison between the calculated stagnation point radiative heat fluxes at $\rho_\infty = 10^{-4}$ kg/m^3 and $V = 10$ and 12 km/s obtained in the present work and those by Tauber and Sutton.[27]

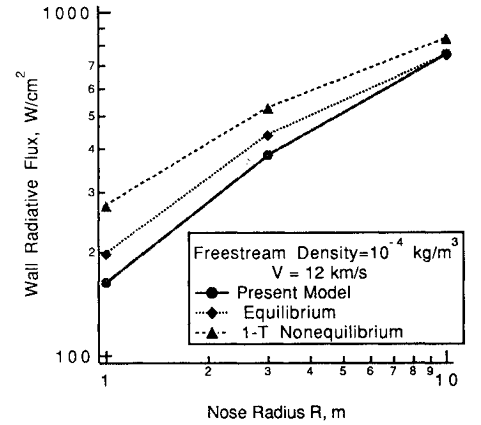

Fig. 19 Comparison between the stagnation point radiative heat fluxes at $\rho_\infty = 10^{-4}$ kg/m^3 and $V = 12$ km/s calculated by the present model, the equilibrium model, and the one-temperature nonequilibrium model for nose radius of 1, 3, and 10 m.

The one-temperature nonequilibrium case leads to such a high flux value because of the high vibrational-electronic temperature immediately behind the shock wave calculated by the one-temperature model (see Fig. 10a).

Sutton and Hartung[26] calculated the magnitudes of the radiative heat flux along the stagnation streamline of blunt bodies of given radius and freestream conditions in air under the assumption of equilibrium. The calculation fully accounted for the effect of radiative cooling, but the boundary layer was not accounted for, and the radiative transport calculation was performed using a simplified method in which molecular bands are represented by continua. Tauber and Sutton[27] derived an analytical expression that approximates the calculated values over the range of nose radii smaller than about 3 m. In Fig. 18, the present results are compared with the Tauber-Sutton formula for the freestream density of 10^{-4} kg/m^3 and the flight speeds of 10 and 12 km/s for the nose radii of 1, 3, and 10 m, though the radius of 10 m is outside of applicability of the expression. Comparison is made with the analytical expression rather than the original data because the former is more convenient. The nose radius of 3 m is of interest because it is the approximate nose radius of the Apollo vehicle, and may be the radius also for future manned Mars-return vehicles.

For the 10 km/s case, the radiative heat fluxes predicted by Tauber and Sutton[27] are higher than the present results. In particular, for $R = 1$ m, the Tauber-Sutton value is nearly twice that of the present calculation. Since radiation overshoot is a dominant phenomenon at 10 km/s (see Fig. 14), and since the Tauber-Sutton calculation fully accounts for radiative cooling, the Tauber-Sutton values are expected to be generally lower than the present values. This inconsistency may be attributed to the radiation absorption in the boundary layer, which was accounted for in the present calculation but not in Ref. 27, and the difference in the details of radiative transport calculations.

For the 12 km/s case, the present result is lower for 1-m nose radius, but nearly the same for the larger nose radii. The agreement for the larger nose radii is expected: the thickness of the nonequilibrium region is negligibly small compared with the thickness of the shock layer for the 10-m nose radius case, and therefore, the flow may be considered to be in equilibrium at 12 km/s. For the 1-m nose radius, the nonequilibrium value is lower than the equilibrium value, probably because the nonequilibrium region emits less atomic radiation.

In Fig. 19, the stagnation point wall radiative flux values are compared for $V = 12$ km/s among the present model, the equilibrium model, and the one-temperature nonequilibrium model, for the nose radii of 1, 3, and 10 m. For $R = 1$ m, there are appreciable differences in the flux value among the three models. However, at $R = 10$ m, the difference becomes relatively small. The equilibrium flux becomes the same as the present model value at $R = 10$ m. The one-temperature flux value (837 W/cm^2) is about 80 W/cm^2 higher than the present model value (756 W/cm^2) at $R = 10$ m.

The analysis leads one to believe that ionic equilibration processes in air at entry velocities above 11 km/s can be described reasonably accurately by using the reaction rate coefficient set derived in the present work. For a nose radius of 3 m or greater, the flow behind the shock wave can be considered to be in thermochemical equilibrium for the purpose of determining radiative heat flux to the wall. As Fig. 18 shows, the radiative heat flux reaching the wall is of the order of several hundred W/cm^2 at the entry velocity of 12 km/s for a nose radius of 3 m or greater. Existing nonablating heat shields, such as those used for the Space Shuttle Orbiter, can withstand a total heating rate of about 50 W/cm^2. Even with a significant future improvement in the performance of the nonablating heat shields, the radiative heat transfer rates predicted here cannot be expected to be withstood by a nonablating heat shield.

Reactions in Ablation Layer

Since the radiative heat transfer rates reaching the wall in a typical super-escape velocity entry is greater than that which can be withstood by a nonablating heat shield, one must consider an ablative heat shield for super-escape velocity entry vehicles. In the ablation process, the radiative heat incident on the wall is absorbed by the latent heat of vaporization and subsequent gas-phase decomposition of the ablation product. The ablation product displaces the boundary layer, as indicated schematically in Fig. 20. The layer of the ablation-product vapor so formed is commonly referred to as ablation-product layer, or simply ablation layer.

Ablative heat shields are typically made of carbonaceous material, containing mostly carbon and hydrogen, or silica (SiO_2), or both (e.g., Ref. 28). The composition of the ablation product at the ablating wall can be calculated from the chemical equilibrium relationship between the surface and the gas phase, and among the different species in the gas phase. The ablation products from a carbonaceous heat shield consist mostly of C_3, and varying amounts of C_2, C, C_3H, C_2H, CH, H, and H_2.[29] The silica heat shield produces SiO, O, and O_2.[30] If hydrocarbons and silica are used simultaneously, as they were for the Apollo vehicle, SiC, SiN, and SiH will also be formed. Many of these gases have known radiation absorption or emission features.[31–47] As these gases travel outward toward the shock wave (see Fig. 20), they are heated by both the absorption of radiation and conduction. This leads to their thermal decomposition. For example, a heat shield made of graphite will produce an ablation-product vapor consisting mostly of C_3, a small amount of C_2, and a minute amount of C. The energy of vaporization of C_3 is 65 kcal/(mole of carbon atoms). As this mixture is heated in the gas phase, C_3 will decompose into $C_2 + C$, and the C_2 will eventually decompose into $C + C$. These decomposition processes cool the ablation layer by absorbing a total of 103 kcal/(mole of carbon atom) of energy. As seen in this example, the heat absorbed during the decomposition process is generally of the same order of magnitude as the heat of vaporization. If, for some reason, the decomposition does not occur, the effectiveness of the heat shield material is correspondingly reduced. Near the edge of the ablation layer, i.e., the region where the ablation product gases mix with the inviscid shock layer flow (see Fig. 20), the ablation product gases may become sufficiently hot to radiate significantly. Atomic carbon and silicon are known to radiate strongly at relatively low temperatures, beginning typically at 5000 K for silicon, and 6000 K for carbon. Such radiation will increase the ablation rate, and thereby lower the effectiveness of the ablative heat shield.

For these reasons, the effectiveness of an ablative heat shield is sensitive to the chemical state of the ablation-product gas. A question arises as to whether the residence times of the species in the ablation-product layer are sufficiently long for the flow to reach chemical equilibrium. To answer this question, let us consider the stagnation region only. In the stagnation region, the conservation equation can be written using the classical boundary-layer theory.[48] Following this theory, the length coordinates along and perpendicular to the wall are first transformed to dimensionless coordinates, usually called ξ and η, which vary from zero to a value of the order unity. Then f and the mass fraction of the species produced α are introduced. Under the assumption of unit Lewis number, the conservation equations can be written for these normalized variables approximately as[48,49]

$$\left(\frac{1}{Sc}\frac{\rho\mu}{\rho_e\mu_e}\alpha'\right)' + f\alpha' = \left(\alpha_e \Big/ 2\frac{du_e}{dr}\right)(W_f - W_r) \qquad (9)$$

where Sc is the Schmidt number, W_f and W_r are the normalized forward and reverse rates of formation of the species α in the units of s^{-1}, du/dr is the tangential velocity gradient, and the subscript e denotes the conditions at the edge of the ablation layer. The differentiation is with respect to η. According to the Newtonian theory for a hemisphere, du_e/dr is given approximately by

$$\frac{du_e}{dr} = \frac{V}{R}\sqrt{\frac{2\rho_1}{\rho_s}} \approx 0.5\frac{V}{R}$$

The quantity f has a magnitude of the order of unity, and therefore, the magnitude of the left side of Eq. (9) is of the order of α_e. Therefore, the right side of Eq. (9) must also be of the order of α_e. To satisfy this requirement, when the forward and the reverse production rates W_f and W_r are both larger than unity, they must be nearly equal in magnitude, that is, the flow must be nearly in equilibrium. Thus, the magnitude of the quantity

$$D_a = (R/V)W_f \qquad (10)$$

is a measure of how close the flow is to equilibrium: the larger the D_a, the closer is the flow to equilibrium. The quantity D_a can be regarded as the Damköhler number characterizing the ablation-product layer.

The characteristic Damköhler number can be estimated from the temperatures and pressures expected within the ablation-product layer. The decomposition processes of most interest are

$$C_3 + M \rightarrow C_2 + C + M - 174\ \text{kcal/mole} \qquad (11)$$

$$C_2 + M \rightarrow C + C + M - 142\ \text{kcal/mole} \qquad (12)$$

$$SiO + M \rightarrow Si + O + M - 190\ \text{kcal/mole} \qquad (13)$$

The rate coefficients for these processes are estimated by assuming the pre-exponential factor C to be 4×10^{14}, the power n to be 0, and T_d to be the reaction energy divided by the universal gas constant. The C and the n values chosen are those of typical such reactions.[50] Pressure is taken to be 0.3 atm, a typical value at the perigee of the aerobraking flight.[23] The results are presented in Fig. 21. As the figure shows, the Damköhler numbers for the reactions Eqs. (11) and (13) are smaller than unity at temperatures below about 10,000 K, implying that the reactions will be in chemical nonequilibrium at these temperatures. Equilibrium is reached only in the region where temperature is higher than 10,000 K. Thus, over a wide region adjacent to the wall, the ablation-product layer will be out of chemical equilibrium. Its consequence on radiation emission and absorption, and resulting wall ablation rate, are unknown at this time.

The problem is made more complicated by the occurrence of turbulence. According to existing evidence, the ablation-product gas mixture emerging from the wall can be turbulent[51] as a result of the nonuniform injection of the ablation products from the wall. The question arises as to how the turbulence behaves in the ablation layer. An attempt to answer this question is made in Ref. 51. In the stagnation region, the absolute magnitude of the shear in the ablation layer caused by the

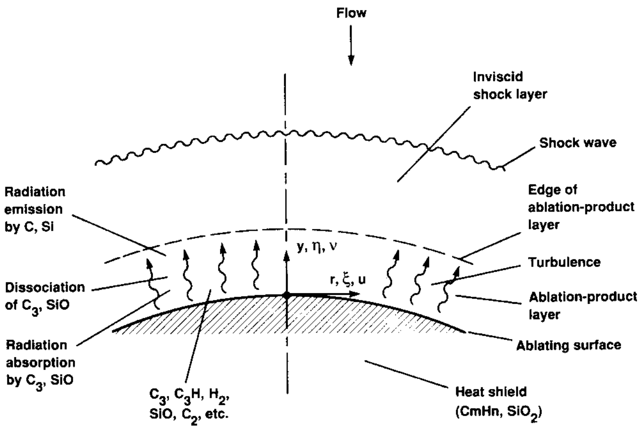

Fig. 20 Schematic of the stagnation region flow phenomena including ablation.

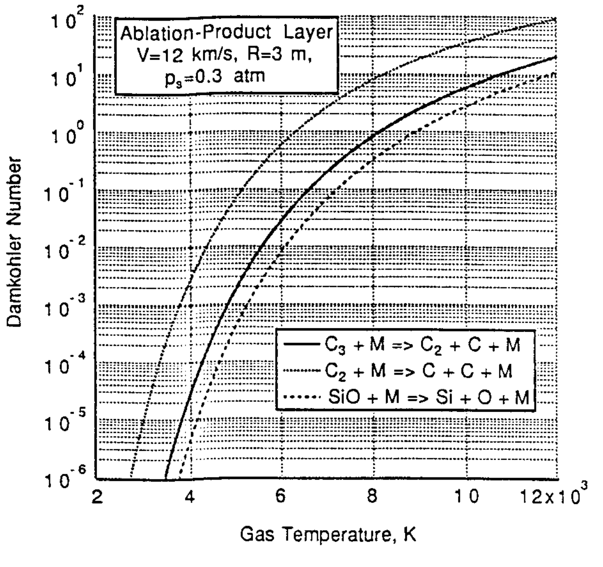

Fig. 21 Calculated Damköhler numbers for the ablation-product layer, for $\rho_\infty = 10^{-4}$ kg/m³, $R = 3$ m, and $V = 12$ km/s.

fluid motion is small. Therefore, the flow turbulence tends to decay in the ablation layer. This behavior is modeled in Ref. 51 by a two-equation turbulence rate model, which is taken from Ref. 52, with the rate of turbulence production set to zero. ε is expressed using the mixing length theory in the form

$$\varepsilon = 0.4\rho v d$$

By defining the normalized turbulence energy function $h = \varepsilon/\varepsilon_w$, the model theorizes that the variable h satisfies the conservation equation in the normalized coordinates of the form[51]

$$\left[\frac{\rho(\mu_t + \mu)}{\rho_e(\mu_{te} + \mu)} h'\right]' + fh' - Gh^{3/2} = 0$$

where μ_t is the turbulent viscosity and G is given by

$$G = \frac{1}{2d} C_d \left(\frac{\mathrm{d}u_e}{\mathrm{d}r}\right)^{-1} \varepsilon_w^{3/2}$$

with $C_d = 0.1455$. In Ref. 51, the initial (wall) value of d is deduced for carbonaceous heat shield materials from the existing experimental data. It is shown therein that the wall value of the mixing length is quite large. This means that the turbulence caused by the ablation process will be dominant in the flowfield of interest. The turbulence will cause deeper penetration of the ablation product into the hot inviscid shock layer region. This will lead to a presence of carbon or silicon atoms in the hot region, which may possibly cause an increase in the radiative heating rate. Such problems must be investigated in the future.

Conclusions

1) The observed ionization behavior behind a normal shock wave in air at super-escape velocities is reproduced fairly well using a set of ionization rate coefficients given in the present work.

2) At the shock layer pressure of the order of 0.15 atm, the thermochemical nonequilibrium phenomena are finished within about 1.5 cm at a flight speed of 12 km/s.

3) Radiation intensity emitted from the nonequilibrium region is less than that emitted from the equilibrium region in the super-escape velocity ranges, i.e., radiation undershoot occurs.

4) For a body of nose radius of 1 m, the nonequilibrium radiation is substantially smaller than the equilibrium radiation. For a body radius of 3 m or larger, the radiative heat transfer rates calculated accounting for the thermochemical nonequilibrium are nearly the same as those obtained assuming equilibrium.

5) At super-escape entry speeds, nearly half or more of the radiative heat flux reaching the wall is contained in the wavelength range below 2000 Å.

6) The conventional one-temperature nonequilibrium model underestimates the thickness of the nonequilibrium region behind the shock wave and overestimates the radiative heat fluxes reaching the wall.

7) The radiative heat flux incident on the stagnation point of a vehicle at a typical super-escape velocity entry flight is sufficiently high to cause ablation at its peak radiation point in its entry trajectory.

8) The ablation-product layer is likely to be turbulent and in a nonequilibrium state.

References

[1] Millikan, R. C., and White, D. R., "Systematics of Vibrational Relaxation," *Journal of Chemical Physics*, Vol. 39, No. 12, 1963, pp. 3209–3213.

[2] Allen, R. A., "Nonequilibrium and Equilibrium Radiation at Super-Satellite Entry Velocities," Avco-Everett Research Lab., Res. Rept. 112, Everett, MA, Oct. 1961.

[3] Park, C., "Problem of Rate Chemistry in the Flight Regimes of Aeroassisted Orbital Transfer Vehicles," *Thermal Design of Aeroassisted Orbital Transfer Vehicles*, edited by H. F. Nelson, Vol. 96, Progress in Astronautics and Aeronautics, AIAA, New York, 1985, pp. 511–537.

[4] Park, C., "Convergence of Computation of Chemically Reacting Flows," *Thermophysical Aspects of Re-Entry Flows*, edited by J. N. Moss and C. D. Scott, Vol. 103, Progress in Astronautics and Aeronautics, AIAA, New York, 1986, pp. 478–513.

[5] Park, C., "Calculation of Nonequilibrium Radiation in the Flight Regimes of Aeroassisted Orbital Transfer Vehicles," *Thermal Design of Aeroassisted Orbital Transfer Vehicles*, edited by H. F. Nelson, Vol. 96, Progress in Astronautics and Aeronautics, AIAA, New York, 1985, pp. 395–418.

[6] Park, C., "Assessment of Two-Temperature Kinetic Model for Dissociating and Weakly-Ionizing Nitrogen," *Journal of Thermophysics and Heat Transfer*, Vol. 2, No. 1, 1988, pp. 8–16.

[7] Park, C., "Assessment of Two-Temperature Kinetic Model for Ionizing Air," *Journal of Thermophysics and Heat Transfer*, Vol. 3, No. 3, 1989, pp. 233–244.

[8] Park, C., "A Review of Reaction Rates in High Temperature Air," AIAA Paper 89-1740, June 1989.

[9] Sharma, S. P., Gillespie, W. D., and Meyer, S. A., "Shock Front Radiation Measurements in Air," AIAA Paper 91-0573, Jan. 1991.

[10] Whiting, E. E., and Park, C., "Radiative Heating at the Stagnation Point of the Aeroassist Flight Experiment Vehicle," NASA TM 102829, Nov. 1990.

[11] Candler, G. V., and MacCormack, R. W., "The Computation of Hypersonic Ionized Flows in Chemical and Thermal Nonequilibrium," AIAA Paper 88-0511, Jan. 1988.

[12] Gnoffo, P. A., Gupta, R. N., and Shinn, J. L., "Conservation Equations and Physical Models for Hypersonic Air Flows in Thermal and Chemical Nonequilibrium," NASA TP 2867, Feb. 1989.

[13] Wilson, J. F., "Ionization Rate of Air Behind High-Speed Shock Waves," *Physics of Fluids*, Vol. 9, No. 10, 1966, pp. 1913–1921.

[14] Park, C., *Nonequilibrium Hypersonic Aerothermodynamics*, Wiley, New York, 1990.

[15] Eckstrom, D. J., "Vibrational Relaxation of Shock-Heated N_2 by Atomic Oxygen Using the IR Tracer Method," *Journal of Chemical Physics*, Vol. 59, No. 6, 1973, pp. 2787–2795.

[16] Kiefer, J. H., and Lutz, R. W., "The Effect of Oxygen Atoms on the Vibrational Relaxation of Oxygen," *Proceedings of the 11th Symposium (International) on Combustion*, Combustion Inst., Pittsburgh, PA, 1967, pp. 67–76.

[17] Wray, K., "Shock-Tube Study of the Vibrational Relaxation of Nitric Oxide," *Journal of Chemical Physics*, Vol. 36, No. 10, 1962, pp. 2597–2603.

[18] Sharma, S. P., and Park, C., "Operating Characteristics of 60-cm and 10-cm Electric Arc-Driven Shock Tubes, Part 2: The Driven Section," *Journal of Thermophysics and Heat Transfer*, Vol. 4, No. 3, 1990, pp. 266–272.

[19] Diblet, B., and Blackman, V. H., "An Approximate Measurement of the Ionization Time Behind Shock Waves in Air," *Journal of Fluid Mechanics*, Vol. 4, Pt. 2, June 1958, pp. 191–194.

[20] Manheimer-Timnat, Y., and Low, W., "Electron Density and Ionization Rate in Thermally Ionized Gases Produced by Medium Strength Shock Waves," *Journal of Fluid Mechanics*, Vol. 6, Pt. 3, Oct. 1959, pp. 449–461.

[21] Lin, S. C., Neal, R. A., and Fyfe, W. I., "Rate of Ionization Behind Shock Waves in Air. I. Experimental Results," *Physics of Fluids*, Vol. 5, No. 12, 1962, pp. 1633–1648.

[22] Frohn, A., and De Boer, P. C. T., "Measurement of Ionization Relaxation Times in Shock Tubes," *Physics of Fluids Supplement I*, 1969, pp. I-54–I-57.

[23] Park, C., and Davies, C. B., "Aerothermodynamics of Sprint-Type Manned Mars Missions," *Journal of Spacecraft and Rockets*, Vol. 27, No. 6, 1990, pp. 589–596.

[24] Allen, R. A., "Nonequilibrium Shock Front Rotational, Vibrational, and Electronic Temperature Measurements," Avco-Everett Research Lab., Res. Rept. 186, Everett, MA, Aug. 1964.

[25] Sharma, S. P., and Gillespie, W., "Nonequilibrium and Equilibrium Shock Front Radiation Measurements," AIAA Paper 90-0139, Jan. 1990.

[26] Sutton, K., and Hartung, L. C., "Equilibrium Radiative Heating Tables for Earth Entry," NASA TM 102652, May 1990.

[27] Tauber, M. E., and Sutton, K., "Stagnation Point Radiative Heating Relations for Earth and Mars Entries," *Journal of Spacecraft and Rockets*, Vol. 28, No. 1, 1991, pp. 40–42.

[28] Bartlett, E. Pl., Anderson, L. W., and Curry, D. M., "An Eval-

uation of Ablation Mechanisms for the Apollo Heat Shield Material," AIAA Paper 69-98, Jan. 1969.

[29]Arnold, J. O., Cooper, D. M., Park, C., and Prakash, S. G., "Line-by-Line Transport Calculations for Jupiter Entry Probes," *Entry Heating and Thermal Protection*, edited by W. B. Olstad, Vol. 69, Progress in Astronautics and Aeronautics, AIAA, New York, 1980, pp. 52–82.

[30]Green, M. J., and Nicolet, W. E., "Aerothermodynamic Environment for Jovian Entry with a Silica Heat Shield," *Outer Planet Entry Heating and Thermal Protection*, edited by R. Viskanta, Vol. 64, Progress in Astronautics and Aeronautics, AIAA, New York, 1979, pp. 108–128.

[31]Cooper, D. M., "Absolute Measurement of the Electronic Transition Moments of Seven Band Systems of the C_2 Molecule," NASA TM 78572, April 1979.

[32]Cooper, D. M., and Jones, J. J., "An Experimental Determination of the Cross Section of the Swings Band System of C_3," *Journal of Quantitative Spectroscopy and Radiative Transfer*, Vol. 22, No. 2, 1979, pp. 201–208.

[33]Jones, J. J., "The Optical Absorption of Triatomic Carbon C_3 for the Wavelength Range 260-560 Nanometers," NASA TP 1141, March 1978.

[34]Prakash, S. G., and Park, C., "Shock Tube Spectroscopy of C_3 + C_2H Mixture in the 140-700 nm Range," AIAA Paper 79-0094, Jan. 1979.

[35]Park, C., and Fujiwara, T., "Shock Tube Study of Silicon-Compound Vapors," *Aerodynamic Heating and Thermal Protection Systems*, edited by L. S. Fletcher, Vol. 59, Progress in Astronautics and Aeronautics, AIAA, New York, 1978, pp. 137–155.

[36]Shinn, J. L., "Optical Absorption of Carbon and Hydrocarbon Species from Shock Heated Acetylene and Methane in the 135-220 nm Wavelength Range," AIAA Paper 81-1189, June 1981.

[37]Prakash, S. G., and Park, C., "Shock-Tube Studies of Atomic Silicon Emission in the Spectral Range of 180 to 300 nm," *Outer Planet Entry Heating and Thermal Protection*, edited by R. Viskanta, Vol. 64, Progress in Astronautics and Aeronautics, AIAA, New York, 1979, pp. 245–264.

[38]Park, C., and Arnold, J. O., "A Shock-Tube Determination of the SiO (A^{Π}-$X^1\Sigma^+$) Transition Moment," *Journal of Quantitative Spectroscopy and Radiative Transfer*, Vol. 19, No. 1, 1977, pp. 1–10.

[39]Park, C., "A Shock-Tube Measurement of the SiO ($E^1\Sigma^+$-$X^2\Sigma^+$) Transition Moment," *Journal of Quantitative Spectroscopy and Radiative Transfer*, Vol. 20, No. 5, 1978, pp. 491–498.

[40]Park, C., "Shock-Tube Determination of Absorption Cross Sections and $A^2\Delta$-$X^2\Pi$ Band Transition Moments of SiH," *Journal of Quantitative Spectroscopy and Radiative Transfer*, Vol. 21, No. 4, 1979, pp. 373–385.

[41]Langhoff, S. R., and Arnold, J. O., "Theoretical Study of the $X^1\Sigma^+$, $A^1\Pi$, $C^1\Sigma^-$, and $E^1\Sigma^+$ States of SiO Molecule," *Journal of Chemical Physics*, Vol. 70, No. 2, 1979, pp. 852–863.

[42]Langhoff, S. R., Bauschlicher, C. W., Jr., Rendell, A. P., and Komornicki, A., "Theoretical Study of the Radiative Lifetime of the $A\ ^1\Pi_u$ State of C_2," *Journal of Chemical Physics*, Vol. 11, No. 1, 1990, pp. 6599–6603.

[43]Langhoff, S. R., and Bauschlicher, C. W., Jr., "Theoretical Study of the $A\ ^3\Sigma^-$-$X\ ^3\Pi$ Transition in SiC," *Journal of Chemical Physics*, Vol. 93, No. 1, 1990, pp. 42–44.

[44]Lewerenz, M., Bruna, P. J., Peyerimhoff, S. D., and Buenker, R. J., "Ab Initio MRD-CI Study of the Electronic Spectrum of SiH," *Molecular Physics*, Vol. 43, No. 1, 1983, pp. 1–24.

[45]Larsson, M., "The $X\ ^3\Pi$, $B\ ^3\Sigma^+$ and $C\ ^3\Pi$ States of SiC According to Ab Initio CASSCF-CCI Calculations," *Journal of Physics B*, Vol. 19, No. 8, 1986, pp. L261–L265.

[46]Chabolowski, C. F., "Ab Initio Study of the Locations and Intensities of the Lowest-Lying Electronic Transitions of the C_3 and C_2O Molecules," *Journal of Chemical Physics*, Vol. 84, No. 1, 1986, pp. 268–274.

[47]Bernath, P. F., Rogers, S. A., O'Brien, L. C., and Brazier, C. R., "Theoretical Predictions and Experimental Detection of the SiC Molecule," *Physical Review Letters*, Vol. 60, No. 3, 1988, pp. 197–199.

[48]Dorrance, W. H., *Viscous Hypersonic Flow*, McGraw-Hill, New York, 1962, pp. 29, 30, 45–56, and 79–88.

[49]Park, C., "Dissociative Relaxation in Viscous Hypersonic Shock Layers," *AIAA Journal*, Vol. 2, No. 7, 1964, pp. 1202–1207.

[50]Beck, W. H., and Mackie, J. C., "Formation and Dissociation of C_2 from High Temperature Pyrolysis of Acetylene," *Journal of Chemical Society: Faraday Transactions I*, Vol. 71, No. 6, 1975, pp. 1363–1371.

[51]Park, C., "Injection-Induced Turbulence in Stagnation-Point Boundary Layers," *AIAA Journal*, Vol. 22, No. 2, 1984, pp. 219–225.

[52]Wassel, A. T., and Denny, V. E., "Heat Transfer to Axisymmetric Bodies in Super- and Hypersonic Turbulent Streams," *Journal of Spacecraft and Rockets*, Vol. 14, No. 4, 1977, pp. 212–218.